


Cite this: *Mater. Adv.*, 2023,
4, 3506Received 8th April 2023,
Accepted 6th July 2023

DOI: 10.1039/d3ma00162h

rsc.li/materials-advances

A comparative study on the photo-removal of a few selected priority organic pollutants in aqueous suspension using vanadium-doped-ZnO/MWCNT†

Mohtaram Danish,‡ Ziyaur Rasool,‡ Haider Iqbal, Reesha Fatima, Shubham Kumar and Mohammad Muneer *

Highly efficient vanadium doped ZnO nano-rods supported with MWCNTs (V@ZnO/MWCNT) have been fabricated using a convenient sol-gel impregnation method. Techniques such as FTIR, XRD, UV-Vis DRS, TEM, and EDX were used to characterize the synthesized pure, doped, and composite materials. The photocatalytic activity of the V@ZnO/MWCNT photocatalysts was tested by studying the degradation of a few selected priority organic pollutants, such as 5-nitroisophthalic, allopurinol, and chloramine-T, in an aqueous medium under UV light in the presence of atmospheric oxygen. Amongst the different synthesized nanocomposite materials, V@ZnO/MWCNT showed the best photocatalytic activity, which was monitored by measuring the change in absorbance at different time intervals using UV-Vis spectroscopic analysis. The kinetics of degradation were examined under varying conditions, such as type of photocatalyst, reaction pH, catalyst dose, substrate concentration, and potassium bromate as an electron acceptor in addition to molecular oxygen. All the compounds under study degraded more effectively under alkaline pH and potassium bromate. Based on the obtained results, a plausible degradation mechanism has been proposed on the irradiated photocatalysts in an aqueous medium and atmospheric oxygen.

1. Introduction

A large number of toxic pollutants are introduced into the water system through different sources, like industrial, pharmaceutical processes, agricultural, and household runoff.^{1–4} These accumulated toxins build up in the aquatic organisms and ultimately make their way into our bodies through the food chain.⁵ The detoxification of this contaminated water is of great concern to society and regulating authorities.⁶ Coagulation, membrane processing, adsorption, ion exchange, and photocatalysis are just some of the techniques utilized during the past few decades to get rid of these harmful substances.⁵ The utilization of semiconducting nanomaterials in photocatalysis has emerged as a highly promising approach for mitigating environmental pollutants. The semiconductor-mediated photopurification of water is well documented in the literature.⁷ The photo-degradation of a wide range of compounds, such as nitro

compounds, amines, surfactants, pesticides, and dyes in the presence of semiconductors in aqueous suspension, is extensively studied. Among the reported materials, numerous nanoparticles and nanocomposites have been produced by scientists, including a few widely used oxides like TiO₂, ZnO, CuO, SnO₂ and CeO₂ etc.^{8–10} Zinc oxide (ZnO) has proven to be one of the most widely accepted and benchmark photocatalysts (for removal of pollutants) owing to its large surface area, oxidizing power, high chemical stability, and low cost.^{3,8,11,12} Earlier studies show that ZnO can effectively oxidize adsorbed compounds when exposed to light and suggest “self-cleaning” characteristics.^{13,14} Several studies involving the removal of organic substances using different types of ZnO have also focused on checking the degradation efficiency in an aqueous system under varying conditions.^{15,16} Unfortunately, its practical usefulness is limited because of its large bandgap and fast back electron transfer. Hence, these two factors are major challenges to the photochemist working in this area.^{17–19} Thus, strategies such as doping and grafting metal and non-metal ions, deposition of noble metal ions, and heterojunction formation are used to minimize the bandgap energy and efficiently use higher wavelength light sources to improve the photonic activity.^{20–24} Recently, vanadium doping onto semiconducting materials has

Department of Chemistry, Aligarh Muslim University, Aligarh-202002, India.

E-mail: readermuneer@gmail.com, m.muneer.ch@amu.ac.in

† Electronic supplementary information (ESI) available. See DOI: <https://doi.org/10.1039/d3ma00162h>

‡ Both authors have equal contributions to this work.



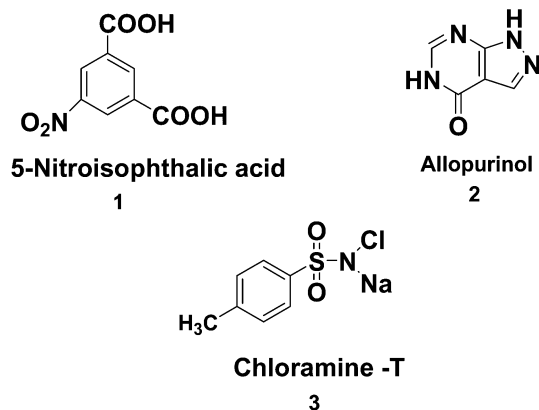


Chart 1 Schematic representation of (1) 5-nitroisophthalic, (2) allopurinol, and (3) chloramine-T.

received significant attention because it can alter the coordination state and the bandgap structure of semiconductor oxides.^{25,26} Metal-doped ZnO nanoparticles have been synthesized using various techniques, such as co-precipitation, sol-gel, and hydrothermal processes.^{27–29} Among these methods, the morphology of the materials could be successively achieved by hydrothermal and sol-gel methods. Nevertheless, the hydrothermal method takes more time and requires more energy to get the nanostructures. Whereas, the sol-gel approach, on the other hand, is an alternative methodology for synthesizing nanosize ZnO in less time, which could be used to produce metal oxide nanostructures.^{30,31} Currently, researchers have also been focusing on multiwalled carbon nanotubes (MWCNTs) due to the efficient adsorption of pollutants on its surface, which could result in high photocatalytic activity.³² A few studies using MWCNTs, such as $\text{MoO}_3/\text{MWCNTs}$,³³ $\text{Co-TiO}_2/\text{MWCNTs}$,³⁴ $\text{MWCNTs-TiO}_2\text{-SiO}_2$ ³⁵ and

$\text{Co-ZnS QDs/g-C}_3\text{N}_4/\text{MWCNTs}$ ³⁶ etc. have recently reported on the development of binary and ternary composites for the removal of pollutants.

Given the potential importance of ZnO and MWCNTs, we have attempted to synthesize a binary nanocomposite, vanadium-doped-ZnO-MWCNTs, with varying mol% (2%, 4% and 6%) of V@ZnO component *via* a thermal impregnation route followed by its characterization using standard techniques such as XRD, FTIR, DRS, SEM/TEM, and XPS. In addition, the activity of the prepared material was accessed by degrading three priority organic pollutants, namely 5-nitroisophthalic acid, allopurinol and chloramine T^{41,42} (Chart 1) in aqueous suspension under UV light in an air atmosphere. A possible photodegradation pathway has also been proposed to better understand the mechanism involved in the degradation of the above-mentioned pollutants.

2. Experimental section

The supplementary file (2.1–2.6) (ESI†) contains the required materials for the fabrication of the catalyst, synthetic procedure, instrumentation involved for characterization of the nanomaterials, degradation procedure and photocatalytic activity of the synthesized photocatalyst.

3. Results and discussion

3.1. XRD study

The XRD technique examined the synthesized materials' composition and crystalline nature. The XRD of the prepared materials is presented in Fig. 1. Fig. 1 shows the XRD spectrum of the MWCNTs showing peaks at $2\theta = 25.84^\circ$ and 42.44° , which correspond to the (002) and (100) planes, and are in good agreement with prior

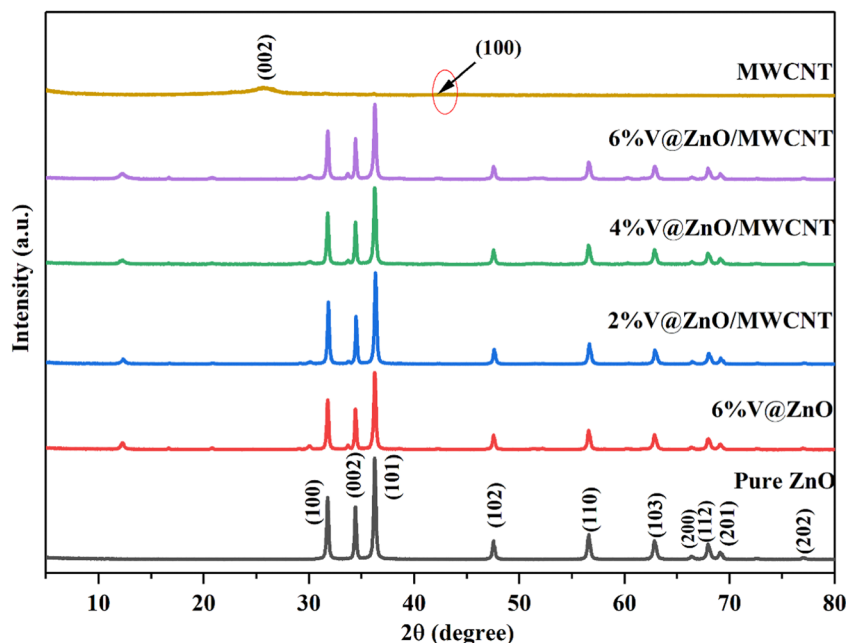


Fig. 1 X-rays of pure ZnO, MWCNTs, 6% V@ZnO and different mol% (2%, 4% & 6%) of V@ZnO/MWCNT nanocomposites.



Table 1 The synthesized materials with crystallite size and crystallinity percentage

S.No.	Sample	Crystallite size (nm)	Crystallinity percentage (%)
1.	MWCNT	—	—
2.	Pure ZnO	56	94
3.	6% V@ZnO	53	85
4.	2% V@ZnO/MWCNT	46	74
5.	4% V@ZnO/MWCNT	42	71
6.	6% V@ZnO/MWCNT	38	69

reports.^{37,38} In the XRD spectrum of pure ZnO, the peaks that appeared at 31.76, 34.42, 36.24, 47.54, 56.62, 62.84, 66.36, 67.94, 69.08, and 76.92 could be attributed to (100), (002), (101), (102), (110), (103), (200), (112), (201), and (202) hexagonal wurtzite ZnO crystal planes, respectively.^{39,40} As the percentage of vanadium metal ion doping was increased, a monotonic decrease in the XRD peak intensity of ZnO was observed, which may be accredited to a minor decrease in crystallinity.²⁷ All peaks corresponding to pure and doped materials were observed in the composite materials, suggesting the successful formation of a V@ZnO/MWCNT heterojunction. Moreover, no peaks corresponding to impurities were detected, signifying the purity of the synthesized materials.

The Scherrer formula was utilized to determine the crystallite size of the prepared materials using XRD data and eqn (1).

$$D = K\lambda/\beta \cos \theta \quad (1)$$

The aforementioned equation involves the utilization of four variables, namely D , K , λ , and β . These variables correspond to the crystallite size, the Scherrer constant (whose value is 0.94), the wavelength of X-ray radiation (which is 0.15418), and the FWHM (full-width half-maxima), respectively. Table 1 displays the calculated crystallite size and the percentage of crystallinity for the

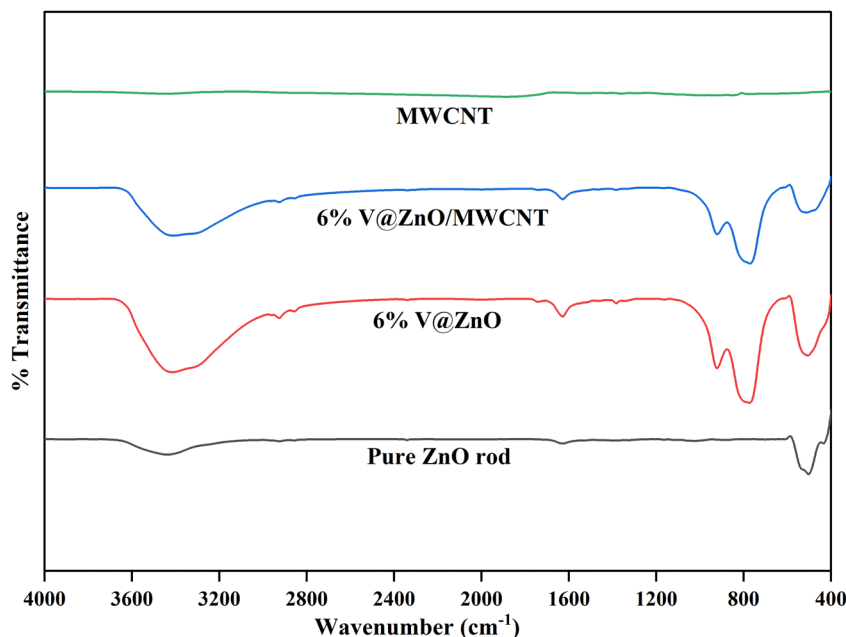
synthesized nanoparticles. The decrease in crystallite size has been noted to be directly proportional to the concentration of V ions. Exceeding the optimal concentration of metal ions in doping may impede the growth of crystallites. Furthermore, the existence of Ni particles within the crystallites may plausibly govern the growth of the crystallites through repulsion, resulting in a reduction in particle size. The enhanced photocatalytic degradation performance can be attributed to the larger surface area of smaller crystallite sizes, which allows for increased adsorption of pollutants. The analysis determined that the size of the crystallites ranged from 38 to 56 nanometers with an error limit of ± 1 nm.

3.2. FTIR analysis

The FTIR analysis of the synthesized materials was recorded in the range of 400–4000 cm^{-1} to identify their chemical structure and bonding interaction. Fig. 2 shows the FTIR spectra of pure ZnO, pure MWCNT, 6% V@ZnO and the 6% V@ZnO/MWCNT nanocomposite. ZnO nanoparticles showed absorption peaks at 3415 cm^{-1} and 1626 cm^{-1} attributed to the stretching and bending vibrations of water molecules that were adsorbed on the catalyst's surface, respectively.^{41,42} A strong band at 508 cm^{-1} could be ascribed to the Zn-O bond characteristic of the hexagonal wurtzite phase of pure ZnO.^{41,43} It has been determined that introducing vanadium into the ZnO lattice is responsible for the appearance of a band with identical characteristics at 768 cm^{-1} and 920 cm^{-1} (Fig. 2).⁴⁴ Furthermore, due to the low contents of MWCNT in V@ZnO, it is difficult to identify the bands of this catalyst in the composite material. No other impurity peaks related to other groups are observed, showing our synthesized sample's purity.

3.3. DRS analysis

The optical characteristics of the synthesized materials were studied with UV-Vis DRS analysis from 250 to 800 nm, as shown

**Fig. 2** FTIR spectra of pure ZnO rod, MWCNTs, 6% V@ZnO and the 6% V@ZnO/MWCNT nanocomposite.

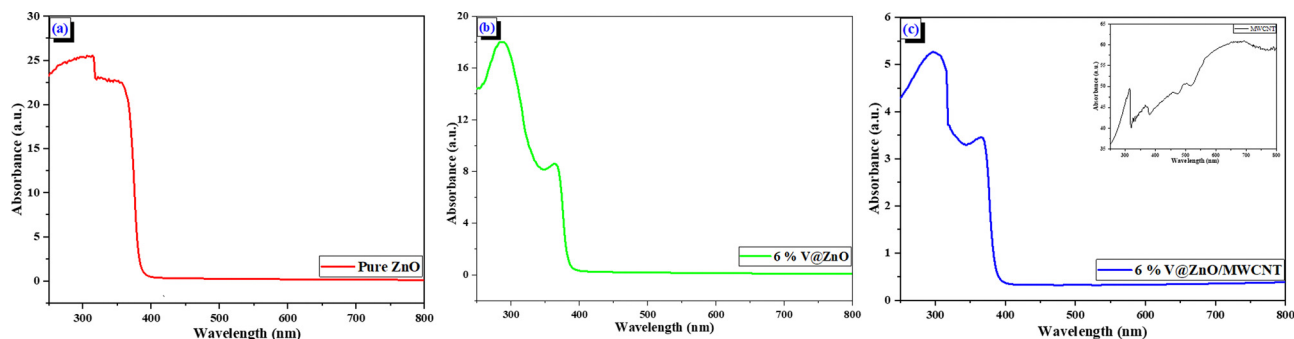


Fig. 3 UV-Vis DRS spectra of (a) Pure ZnO, (b) 6% V@ZnO and (c) the 6% V@ZnO/MWCNT nanocomposite (insets of MWCNTs).

in Fig. 3. Since pure ZnO nanorods exhibit an absorption edge at 381 nm, it can only perform when exposed to UV light. Interestingly, it was also observed that the absorption edge of the ZnO nanorod shifted towards higher wavelengths as a function of

vanadium metal ion doping.¹⁸ Furthermore, a bathochromic shift is observed in the ZnO photocatalysts due to the inclusion of vanadium metal ions and MWCNT, which makes the nanocomposite material more active at higher wavelength.²⁷

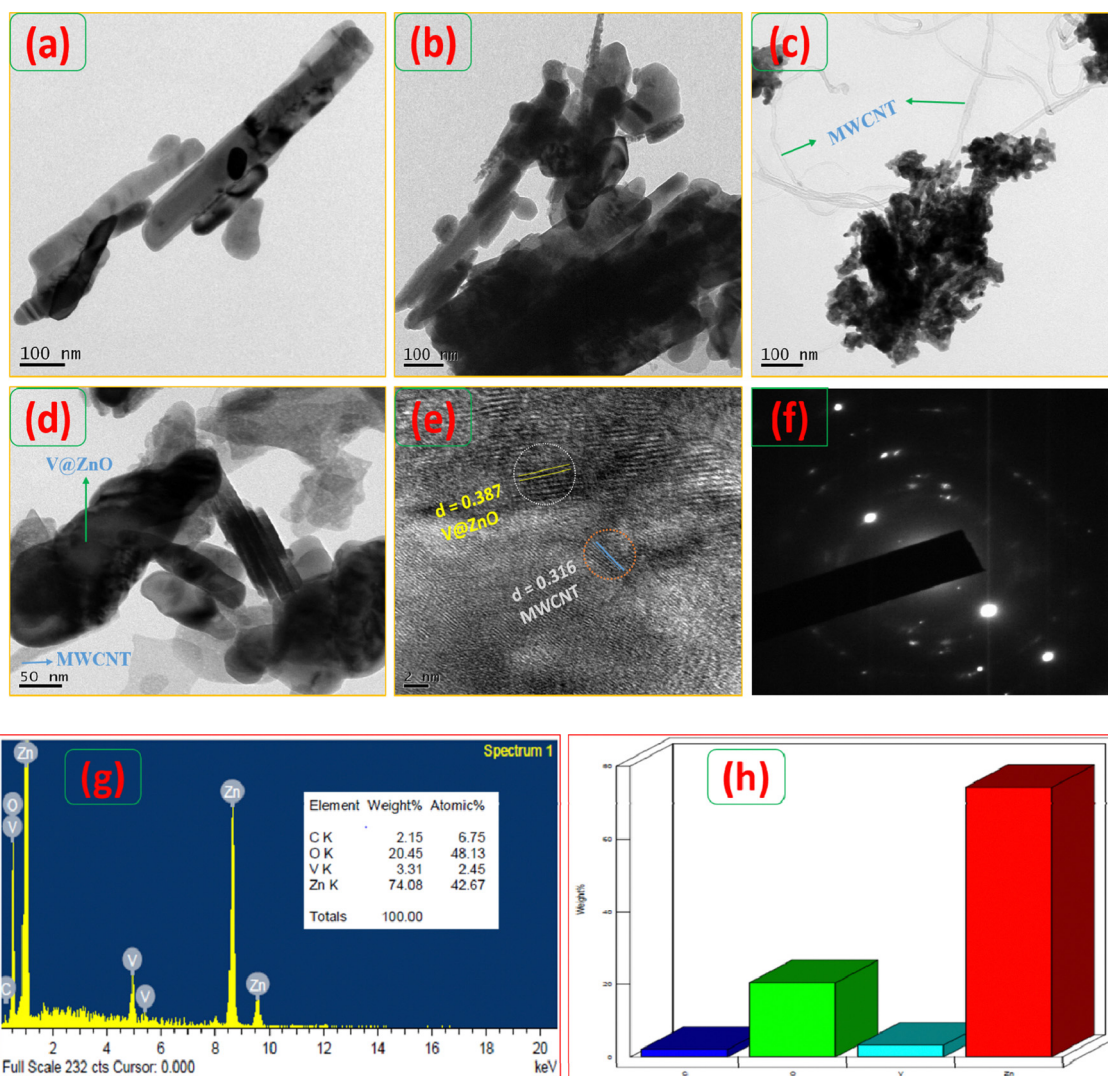
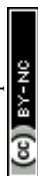


Fig. 4 TEM image of pure ZnO rods (a), 6% V@ZnO (b), pure MWCNTs (c) and 6% V@ZnO/MWCNT (d), HR-TEM image of 6% V@ZnO/MWCNT (e), and selected area electron diffraction (SAED) pattern of the 6% V@ZnO/MWCNT nanocomposite (f). EDX spectra (g) and weight percentage of elements (h) of the 6% V@ZnO/MWCNT nanocomposite.



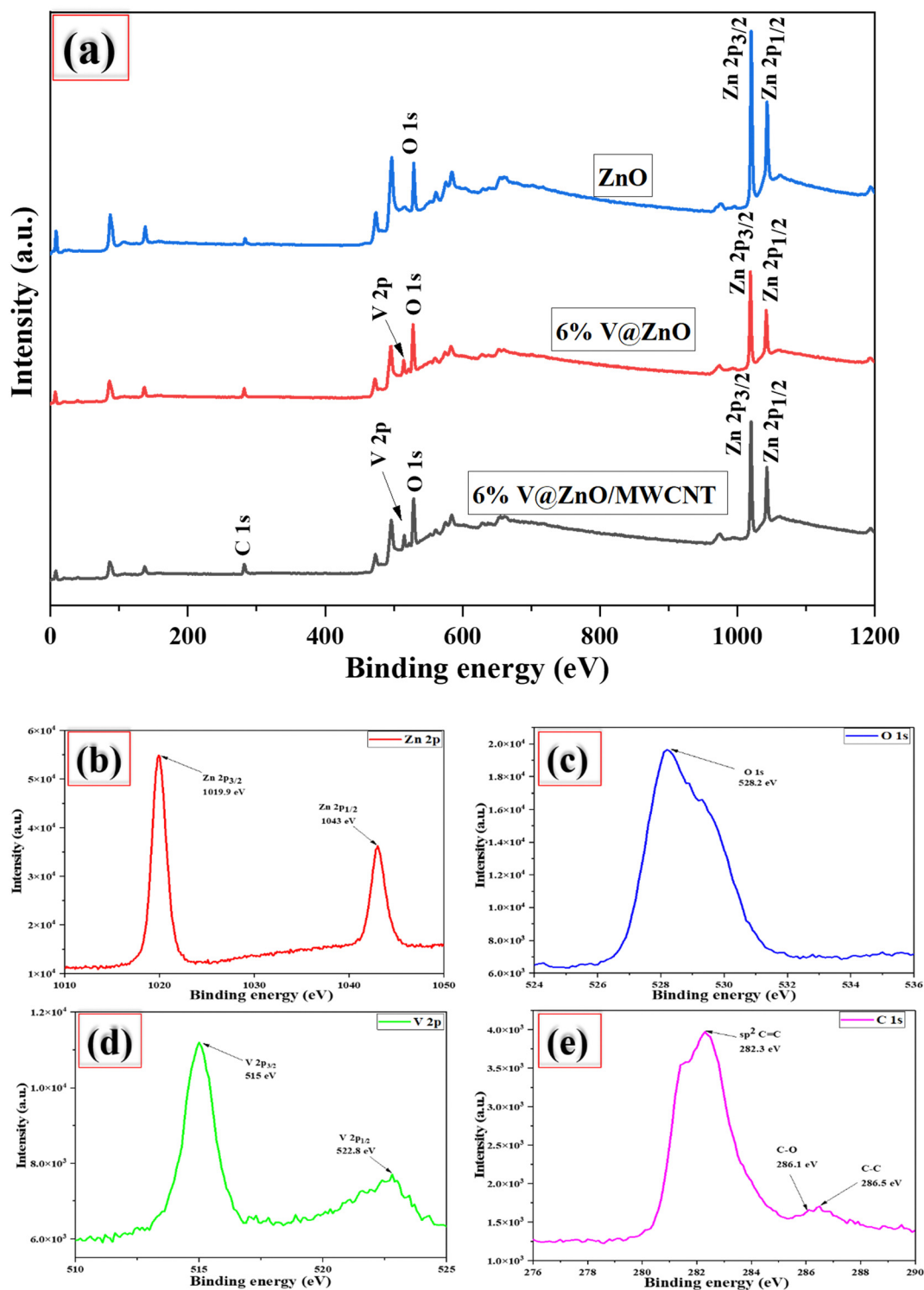


Fig. 5 Full scan survey XPS spectra of ZnO, V@ZnO & the V@ZnO/MWCNT nanocomposite (a); high-resolution spectra of Zn 2p (b), O 1s (c), V 2p (d), and C 1s (e).

3.4. TEM and EDS analysis

TEM and HR-TEM techniques have been performed to analyze the internal morphology of the synthesized nanomaterials (Fig. 4). The rod-like shape image obtained for the pure ZnO is shown in Fig. 4a. Vanadium-doped ZnO nanoparticles also show the same rod-like shape (Fig. 4b) with a rough surface

morphology, which may be due to the aggregation of vanadium particles. A helically shaped bundle of long uniform nanotubes (Fig. 4c) is the typical morphology of MWCNTs. Fig. 4d reveals the successful deposition of V@ZnO onto the surface of the MWCNTs forming a binary nanocomposite. Fig. 4e clearly shows that the synthesized nanocomposite shows good



interface contacts of V@ZnO with the MWCNTs. The single crystalline nature of V@ZnO/MWCNT is demonstrated by the selected area electron diffraction (SAED) patterns, as shown in Fig. 4f. The EDX spectra and weight percentages of elements in the V@ZnO/MWCNT are shown in Fig. 4(g and h). It is evident that all elements exist in the prepared material, and the composition of all elements was determined to be near to that of the weight percent of individual atoms present in a nanocomposite containing V@ZnO/MWCNT.

3.5. XPS analysis

XPS measurements were performed to examine the composition and oxidation state of the most active catalyst (6% V@ZnO/MWCNT). Fig. 5a depicts the full scan survey spectra of V@ZnO/MWCNT, which demonstrate the presence of solely Zn, O, C, and V elements, signifying the purity of the photocatalyst. The peaks in Fig. 5b can be seen to be in agreement with the binding energies of 1019.9 and 1043 eV, assigned to the core levels of Zn 2p_{3/2} and zinc 2p_{1/2}, respectively. This demonstrates the oxidation of Zn²⁺ present in the V@ZnO/MWCNT nanocomposite material and made a covalent Zn-O bond.^{45–50} The energy difference between the two peaks is 23.1 eV, which is consistent with the conventional value of 22.97 eV.⁴⁷ A significant peak in the O 1s signal at binding energy 528.2 eV is caused by the presence of lattice oxygen in the –2 oxidation state (Fig. 5c).^{21,51} Vanadium metal's XPS spectrum reveals two peaks corresponding to 2p_{3/2} and 2p_{1/2} with binding energies of 515 and 522.8 eV, respectively, suggesting the successful incorporation of V into the ZnO lattice (Fig. 5d). The peak for V 2p_{3/2} with +4 oxidation state was determined to be 515 eV, which is in good agreement with previously reported binding energies for V⁴⁺, whereas the chemical state of V 2p_{1/2} is for V⁵⁺.^{27,52,53} After loading MWCNT onto V@ZnO, additional peaks in the C 1s spectra were seen at 282.2, 285.9 and 286.5 eV (Fig. 5e), which correspond to sp² C=C, C–O, and sp³ C–C, respectively.⁵⁴ The peak (sp² C=C) at 282.3 eV is predominantly due to benzene.⁵⁴ In addition to this, the peaks in the MWCNTs that correspond to C–O and C–C may be found at 285.9 eV and 286.5 eV.⁵⁵ The low-intensity carbon-oxygen peaks in C 1s have been observed due to defects in the MWCNTs, which produce O 1s.⁵⁶

Table 2 Comparison of BET-surface area, pore size and pore volume of the synthesized pure ZnO, 6% V@ZnO and 6% V@ZnO/MWCNT nanocomposite

Sample	BET-specific surface area (m ² g ^{−1})	Pore size (nm)	Pore volume (cm ³ (STP) g ^{−1})
ZnO	9.9545	23.831	2.2871
V@ZnO	24.114	27.713	5.5402
V@ZnO/MWCNT	26.934	30.799	6.1882

3.6. BET analysis

The BET-nitrogen adsorption–desorption isotherm of the synthesized pure and composite samples was also performed to determine the different surface parameters.^{57,58} Fig. 6a shows the BET surface area, pore diameter and pore volume of ZnO, V@ZnO and the V@ZnO/MWCNT composite. To characterize the mesoporous structure of the composite material, the enclosed H₃-hysteresis loop has been obtained, which shows a type IV isotherm based upon the IUPAC classifications.⁵⁹ Moreover, the BJH plot (Fig. 6b) gives information about the pore diameter distribution of the particles.⁶⁰ Table 2 comprises these surface characteristics, which exhibits that composite material V@ZnO/MWCNT has a high BET-surface area of 26.934 m² g^{−1} along with a high pore size and pore volume of 30.799 nm and 6.1882 cm³ g^{−1}, respectively in comparison to pure ZnO and V@ZnO nanomaterials. The proliferation in the composite material's surface area, pore diameter and pore volume leads to enhancement in adsorption of organic pollutants for better degradation results.^{36,61}

3.7. Reaction of 5-nitroisophthalic acid (1) with V@ZnO/MWCNT and pure TiO₂ (P25)

An aqueous solution of 5-nitroisophthalic acid (0.4 mM, 140 mL) was irradiated in the presence of different photocatalysts such as V@ZnO/MWCNT and Degussa P25 (1 g L^{−1}) using a 125 W lamp in a pyrex glass reactor with the continuous bubbling of air at different time intervals. Fig. 7a and b show the change in absorbance of 5-nitroisophthalic acid as a function of time over V@ZnO/MWCNT and Degussa P25, respectively. The figure shows the decrease in absorption intensity with time, showing 97% and

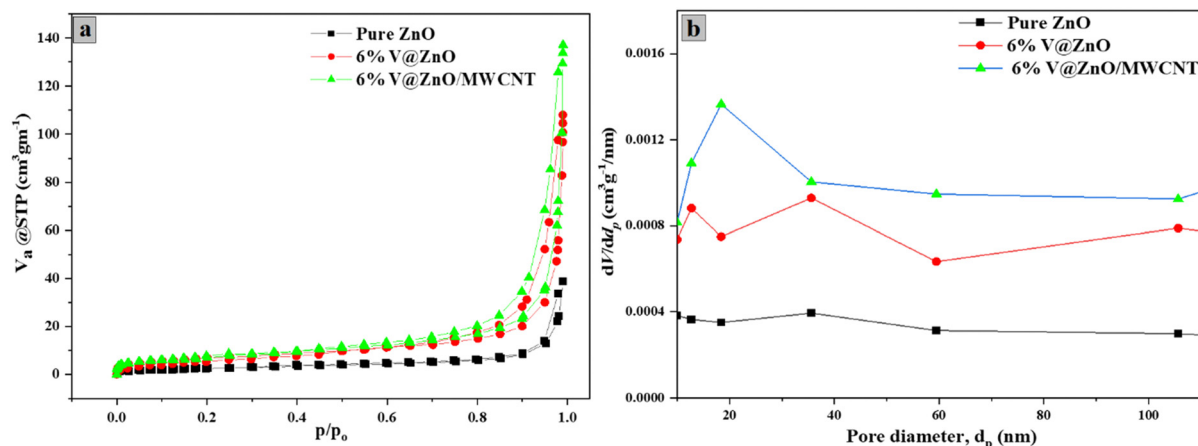


Fig. 6 N₂ adsorption–desorption isotherm (a) and BJH plot for pore size distribution (b) of pure ZnO, V@ZnO and V@ZnO/MWCNT nanocomposites.



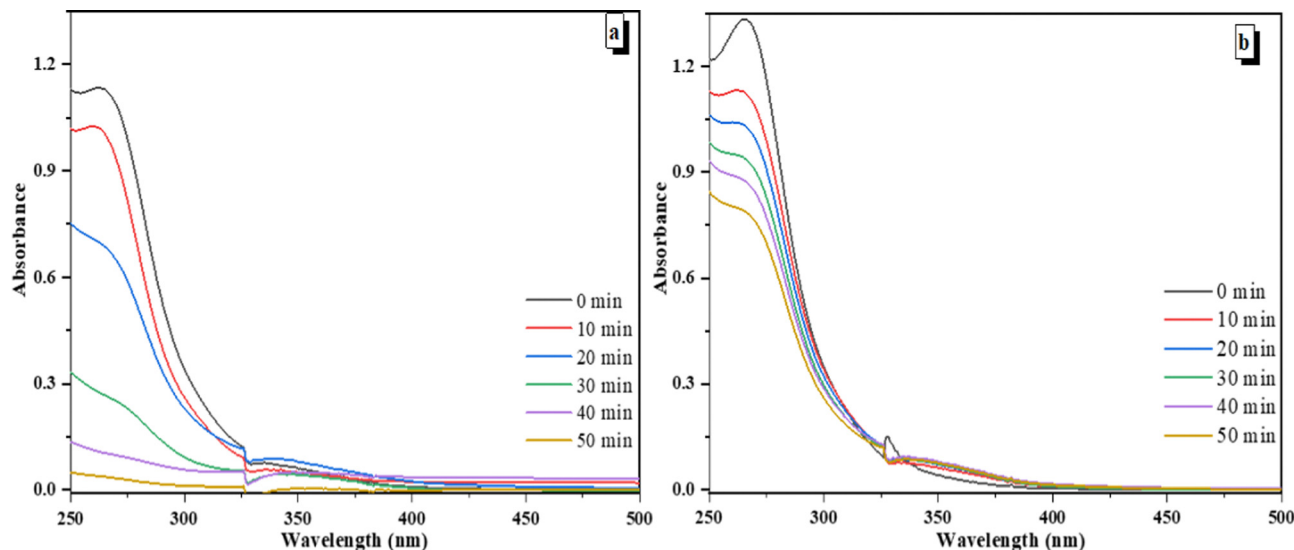


Fig. 7 Decrease in absorbance at 260 nm at different time intervals (a) over V@ZnO/MWCNT, and (b) Degussa P25 on irradiation of an aqueous suspension of 5-nitroisophthalic acid.

40% degradation in 50 min. It was also seen that V@ZnO/MWCNT degrades the 5-nitroisophthalic acid faster than Degussa P25. The improved photodegradation rate of 5-nitroisophthalic acid over V@ZnO/MWCNT could be attributed to efficient light absorption ability and better separation of charge carriers.

3.8. Degradation of 5-nitroisophthalic acid, allopurinol and chloramine-T using different types of TiO₂ and V@ZnO/MWCNT nanocomposite

In heterogeneous reactions, the activity of a catalyst depends on the size and surface area; therefore, the activity of commercially available TiO₂ (Degussa P25, Hombikat UV100 and Millennium Inorganic PC500) and our synthesized V@ZnO/MWCNT, was studied for the decomposition of the compounds mentioned above. Fig. 8 shows the degradation rate of 5-nitroisophthalic acid, allopurinol and chloramine-T using three types of TiO₂ and the synthesized V@ZnO/MWCNT. The figure reveals that the V@ZnO/MWCNT photocatalyst was found to be more effective for the degradation of colorless pollutants, e.g. chloramine-T, 5-nitroisophthalic acid and allopurinol, respectively. The variation in activity could be due to differences in the surface area, lattice mismatches, and distribution of hydroxyl groups on the surface of the catalyst as they influence the adsorption mechanism of a pollutant. Within the experimental limits, the photocatalytic activity of Degussa P25, PC500 and UV100 was more or less similar, with stronger activity observed for Degussa P25. This finding reveals that the behavior of the photocatalysts may also depend on the type of chromophore.

3.9. pH effect on the degradation of 5-nitroisophthalic acid, allopurinol and chloramine-T using the V@ZnO/MWCNT nanocomposite

The pH of the solution is a significant parameter in the photocatalytic reaction on surfaces as it determines the photocatalyst surface charge properties and the scale of the aggregates it produces. The solution pH improves the electrolyte

interface's electrical double layer and thereby affects the adsorption-desorption processes and generation of electron-hole pairs on the surface of the semiconductor. The degradation of 5-nitroisophthalic acid, allopurinol, and chloramine-T was investigated at pH values between 4 and 11 using V@ZnO/MWCNT as a photocatalyst. It is worth mentioning here that the reaction pH was maintained before the irradiation process. The degradation rate of 5-nitroisophthalic acid, allopurinol, and chloramine-T at different pH values is shown in Fig. 9. The rate was found to increase with the increase in the pH of the reaction mixture of 5-nitroisophthalic acid and chloramine-T, and the highest degradation rate was observed at pH 11. Moreover, for allopurinol, a better rate could be seen both

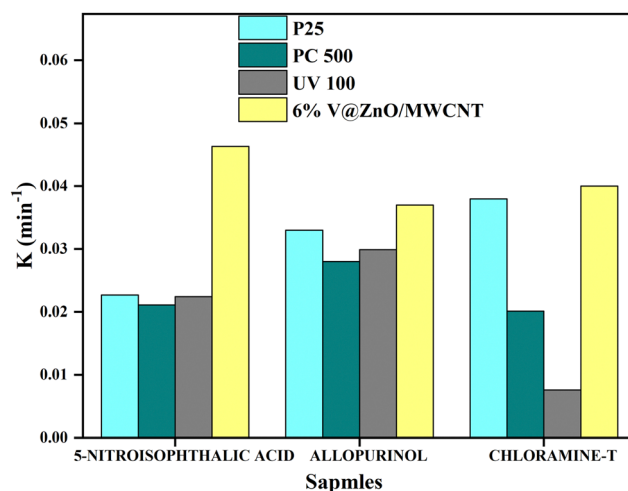


Fig. 8 Rate for the decomposition of 5-nitroisophthalic acid, allopurinol, and chloramine-T with different TiO₂ and the synthesized catalyst. Conditions: concentration (0.4 mM), 125 W medium pressure Hg lamp, TiO₂: Degussa P25 (1 g L⁻¹), Hombikat UV 100 (1 g L⁻¹), PC 500 (1 g L⁻¹) and 6% V@ZnO/MWCNT (1 g L⁻¹), with irradiation time 50 min.



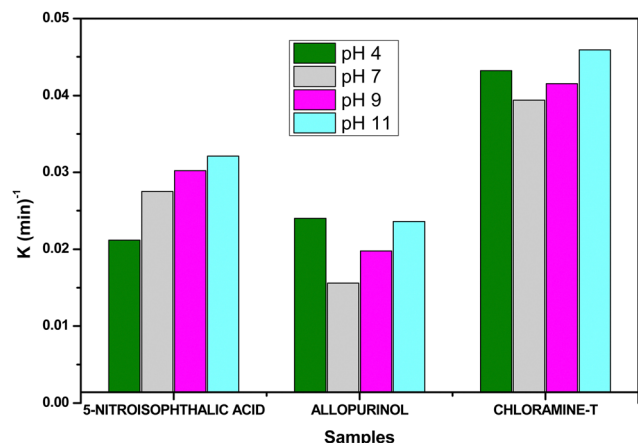


Fig. 9 pH effect on the degradation rate of 5-nitroisophthalic acid, allopurinol, and chloramine-T in aqueous suspension under UV light. Conditions: substrate (0.25 mM), catalyst: 6% V@ZnO/MWCNT (1 g L^{-1}), $V = 140 \text{ mL}$, constant O_2 -purging, time 6 h.

under acidic and alkaline pH and decreased at neutral pH. A more effective generation of hydroxyl radicals by semiconducting nanoparticles might be the reason for a better degradation rate at alkaline pH.

3.10. Catalyst concentration effect on the degradation rate of 5-nitroisophthalic acid, allopurinol, and chloramine-T using the V@ZnO/MWCNT nanocomposite

An appropriate amount of photocatalyst must be determined to prevent excess catalysts and ensure maximum absorption of light photons for effective degradation. The effect of the degradation kinetics of the 5-nitroisophthalic acid, allopurinol, and chloramine-T under study at various concentrations of V@ZnO/MWCNT photocatalyst ($0.5\text{--}4 \text{ g L}^{-1}$) was investigated, and the

results are shown in Fig. 10. As predicted, initially with the increase in catalyst loading up to 2.5 g L^{-1} , the degradation rate was observed to be increased, which is characteristic of heterogeneous photocatalysis. The obtained results showed that the rate of degradation percent of all the compounds increases with the increase of the photocatalyst loading from 0.5 to 2 g L^{-1} because of the increase in the number of active sites that interact with pollutant molecules. But after surpassing the catalyst dose of 2.5 g L^{-1} , the degradation efficiency was not substantially increased; a little reduction in the degradation rate was observed. The decrease in degradation efficiency can be attributed to the excessive loading of catalysts, which leads to the aggregation of free particles of catalysts. This phenomenon results in an increase in the opaqueness of the solution. So, it was obvious that light couldn't get into the solution as the light was scattered by more and more particles. As a consequence, there was a decrease in the formation of active radicals because only a small number of photons were able to reach the active catalyst sites. Hence, the optimum catalyst dose for the photo removal of the given three colorless pollutants will be $6\% \text{ V@ZnO/MWCNT}$.

3.11. Substrate concentration effect on degradation of 5-nitroisophthalic acid, chloramine-T and allopurinol using the V@ZnO/MWCNT nanocomposite

The effect of substrate concentration on the degradation of 5-nitroisophthalic acid, allopurinol, and chloramine-T in the presence of V@ZnO/MWCNT was determined in the range of 0.1 to 0.4 mM to determine the optimal concentration, and the results are shown in Fig. 11. The figure shows a decrease in rate with the increase of the initial concentration, which might be because high concentration prevents the penetration of light intensity into the solution. The other reason could be that

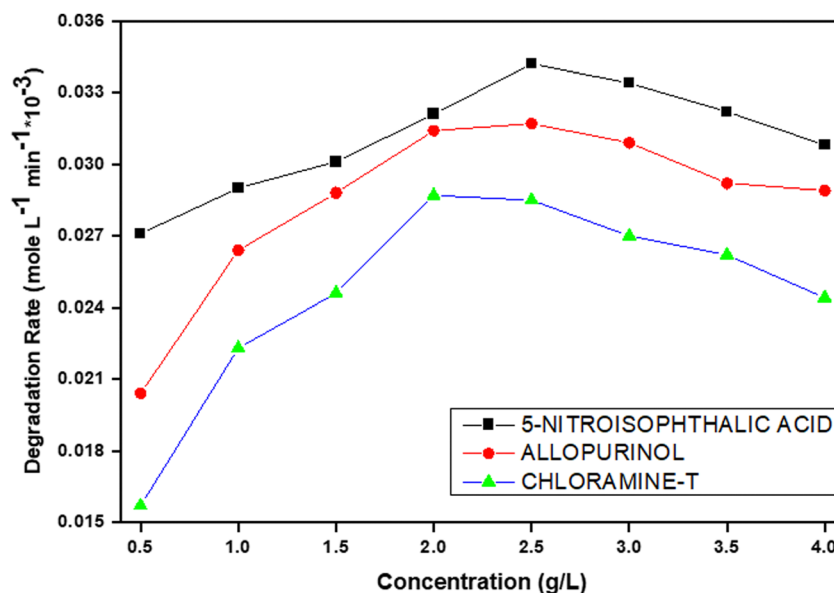


Fig. 10 Catalyst concentration effect on the decomposition rate of 5-nitroisophthalic acid, allopurinol and chloramine-T in aqueous suspension under UV light. Experimental conditions: photocatalyst: $6\% \text{ V@ZnO/MWCNT}$ ($0.5\text{--}4 \text{ g L}^{-1}$), $V = 250 \text{ mL}$, constant O_2 -purging, time 6 h.



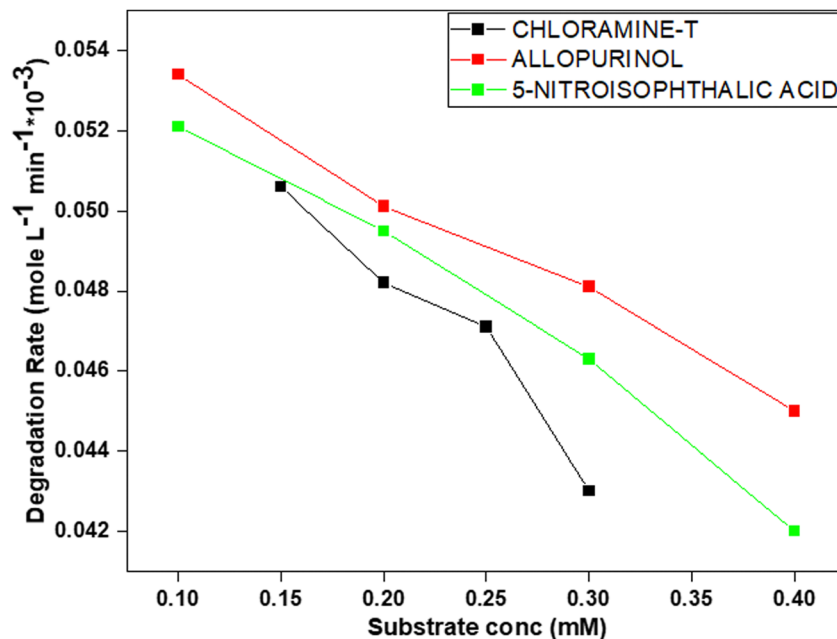


Fig. 11 Substrate concentration effect on the decomposition of 5-nitroisophthalic acid, allopurinol and chloramine-T in aqueous suspension under UV light. Experimental conditions: photocatalyst: 6% V@ZnO/MWCNT (1 g L⁻¹), V = 250 mL, constant O₂-purging, time 6 h.

although more molecules are adsorbed onto the surface of V@ZnO/MWCNT, the generation of reactive species ($\bullet\text{OH}$ and $\text{O}_2^{\bullet-}$ radicals) on the surface of the catalyst remains constant.

3.12. Effect of electron acceptor on the degradation of 5-nitroisophthalic acid, allopurinol, and chloramine-T using the V@ZnO/MWCNT nanocomposite

The undesired electron-hole pair recombination is extremely efficient if there are no proper electron acceptors or donors. This represents the major energy-wasting process and therefore

restricts the achievable quantum performance, which is a drawback from an application point of view in using photocatalysts. Adding other (irreversible) electron acceptors to the reaction is a method to prevent the recombination of the electrons/holes. This may stop electron-hole pair recombination by accepting electrons and producing other oxidizing species, thereby increasing the degradation rate. Therefore, the effect of an electron acceptor, like potassium bromate (KBrO_3), on the rate of 5-nitroisophthalic acid, allopurinol, and chloramine-T under investigation has also been studied. The decomposition rate of 5-nitroisophthalic acid, allopurinol, and

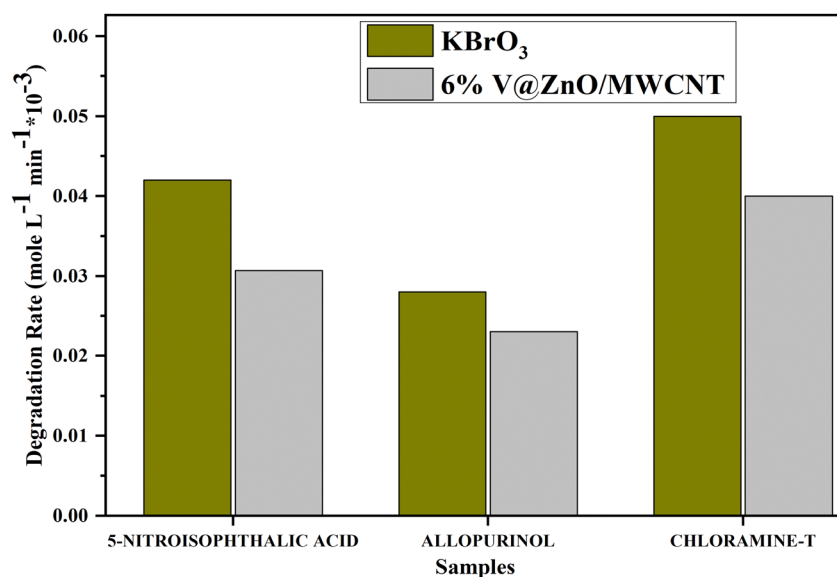


Fig. 12 Electron acceptor effect on the decomposition rate of 5-nitroisophthalic acid, allopurinol and chloramine-T in aqueous suspension under UV light. Experimental conditions: photocatalyst: 6% V@ZnO/MWCNT (1 g L⁻¹), V = 250 mL, constant O₂-purging, time 6 h.



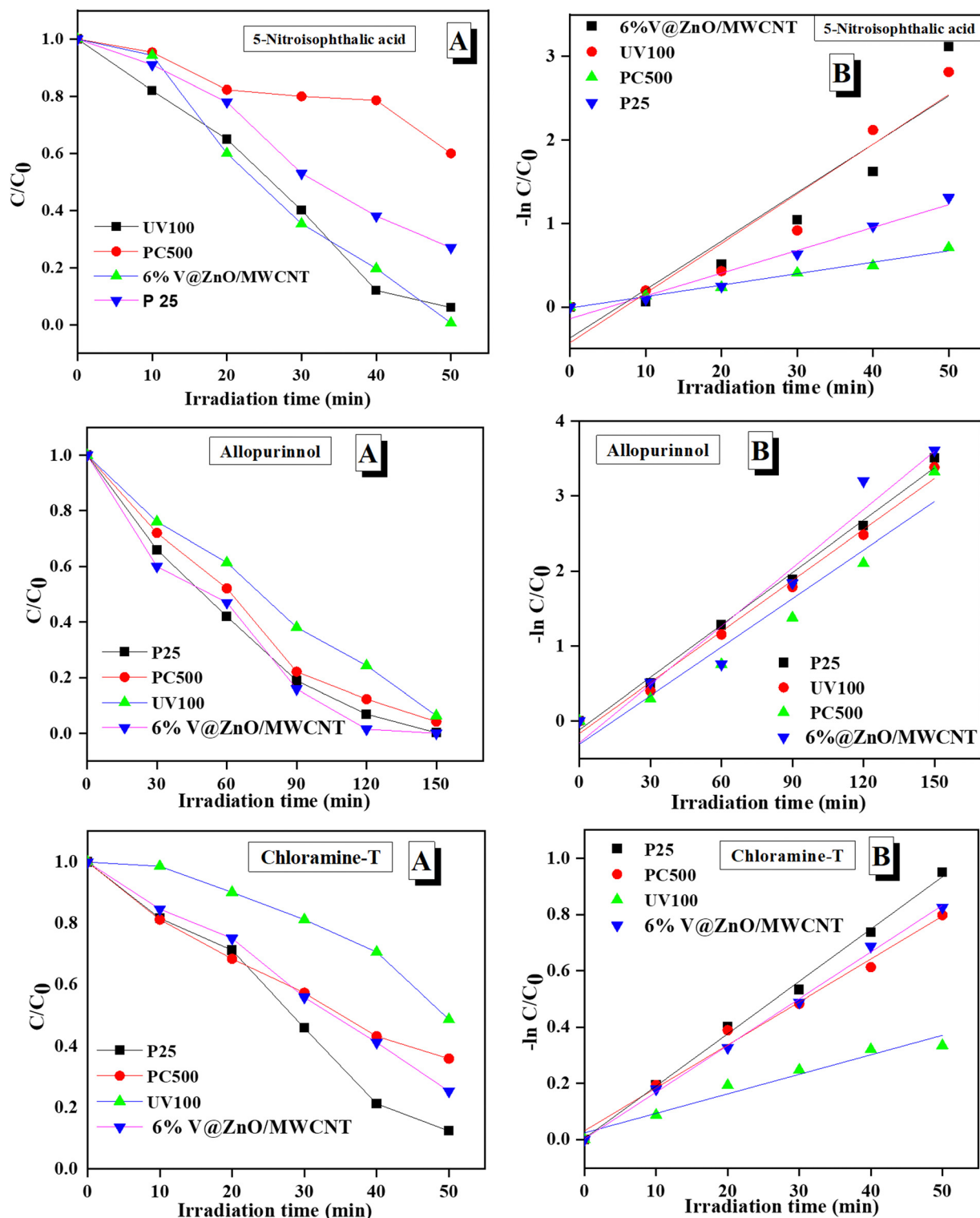
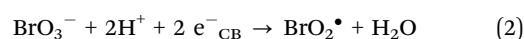
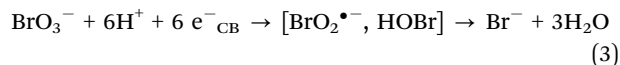


Fig. 13 Change in concentration of three different organic pollutants in the presence of different photocatalysts under a UV light source (a) and the plot between $\ln C/C_0$ vs. irradiation time showing the kinetics study of pollutant degradation (b).

chloramine-T in the absence and presence of an electron acceptor is presented in Fig. 12. It could be seen from the figure that the degradation rate of all compounds under investigation increases in the presence of an electron acceptor like potassium bromate.

An electron acceptor like potassium bromate may produce bromate radicals by accepting a large number of electrons according to the equations given below,





The reduction potentials for the generated reactive species are $E(\text{O}_2/\text{O}_2^{\bullet-}) = -155$ mV and $E(\text{BrO}_3^-/\text{BrO}_2^{\bullet-}) = 1150$ mV. Thermodynamically, the additive used could also be more effective than a molecular oxygen acceptor. A different mechanism could be operative as the reduction of bromide ions does not give hydroxyl radicals but *via* the generation of other oxidizing reagents or reactive radicals such as HOBr and BrO_2^{\bullet} . Also, the bromate ion by itself may act as an oxidizing agent, and a possible degradation route of 4-chlorophenol in the presence of bromate ions has been suggested earlier by Lindner,⁶² indicating the direct oxidation to bromated products. In the case of the model compounds examined in the present work, a similar mechanism may be feasible.

3.13. Photodegradation and degradation kinetics

The concentration of 5-nitroisophthalic acid, allopurinol, and chloramine-T was calculated by a standardized calibration curve obtained at varying concentrations from the absorption of organic contaminants. Fig. 13a reveals that the V@ZnO/MWCNT was found to be more effective for the degradation of chloramine-T, 5-nitroisophthalic acid and allopurinol, respectively. In addition, the degradation kinetics of 5-nitroisophthalic acid, allopurinol, and chloramine-T were also studied by comparing the activity of V@ZnO/MWCNT with other TiO_2 samples using the Langmuir Hinshelwood rate equation. The reaction follows pseudo-first-order kinetics and can be expressed by eqn (4).^{63,64}

$$\ln(C_0/C_t) = kt \quad (4)$$

where C_0 and C_t are the initial and final concentrations at a fixed irradiation time, respectively, and k is the pseudo-first-order rate constant. The curve fits for the degradation of these organic compounds by using different nanoparticles are shown in Fig. 13b. The results show that V@ZnO/MWCNT is the best photocatalyst for the degradation of chloramine-T, 5-nitroisophthalic, and allopurinol, respectively. Therefore, it could be concluded that an appropriate photocatalyst must be required for the selective degradation of organic pollutants.

3.14. Scavenging test

For the determination of leading active species towards photodegradation processes, the scavenging experiment was performed by varying the scavengers like benzoquinone (BQ), isopropyl alcohol (IPA), and disodium ethylenediamine (EDTA-2Na) to quench the ROS such as superoxide ($\text{O}_2^{\bullet-}$) radicals, hydroxyl ($\bullet\text{OH}$) radicals and holes (h^+), which were produced by illuminating the aqueous suspension of 5-nitro isophthalic acid in the presence of our most active photocatalyst 6% V@ZnO/MWCNT. Under the analogous conditions, the performance of the quenchers shows a remarkable reduction in the photocatalytic degradation of pollutants.⁶⁵ Fig. 14 shows the comparison of the percentage degradation of 5-nitro isophthalic acid in the absence & presence of these three different quenchers (BQ, IPA, and EDTA-2Na). The maximum inhibition of the degradation rate from 97%

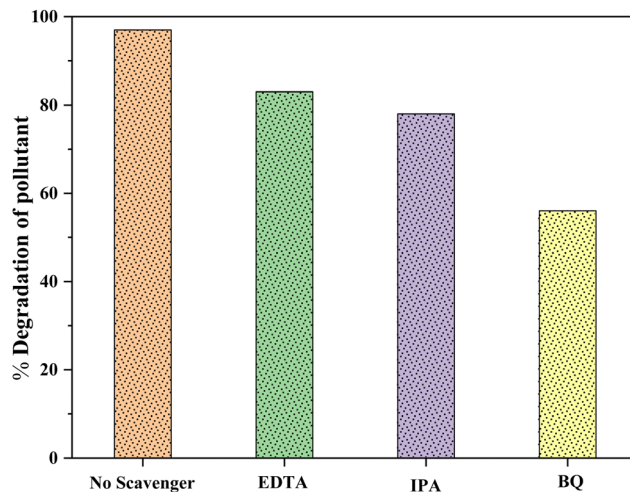


Fig. 14 Effect of different quenchers for the photodegradation of colorless pollutants in the presence of 6% V@ZnO/MWCNT.

to 56% was observed in the presence of BQ, confirming the involvement of superoxide radicals as the most reactive species. Also, in the case of IPA and EDTA-Na_2 , the degradation has been somewhat affected to give 83% and 78% degradation rates, respectively. This provides insight into successfully generating hydroxyl ($\bullet\text{OH}$) radicals and holes (h^+) during this photocatalytic process.

3.15. Catalyst recyclability and stability

Multiple experimental cycles under similar reaction conditions were performed to determine the significance of the stability of our most active catalyst (6% V@ZnO/MWCNT).⁶⁶ Fig. 15a demonstrates the successful recycling of the photocatalyst up to four cycles of photocatalytic degradation. After each consecutive cycle, the exhausted catalyst was filtered, washed with water-ethanol, and dried in a hot air oven overnight, then used for the next photodegradation cycle of one of the colorless pollutants, *e.g.*, 5-nitroisophthalic acid. A slight decrease in the degradation rate is due to some deactivation in the catalytic site of the photocatalyst after four successive cycles. This also exhibits the excellent stability of the 6% V@ZnO/MWCNT photocatalyst, which is important from the application point of view. The photostability of the catalyst was well supported by XRD and FTIR spectra (Fig. 15b and c), recorded before and after the recyclability study, which determined no significant change in the XRD characteristic peaks and in the IR absorption spectra of the photocatalyst.⁶⁷

4. Reaction mechanism

As we know, the phenomenon observed in a semiconductor upon absorption of a photon with energy equal to or exceeding its bandgap energy, involves the excitation of an electron from the valence band (VB) to the conduction band (CB), resulting in the formation of holes in the VB.⁶² As can be seen from Scheme 1, when the 6% V@ZnO/MWCNT nanocomposite



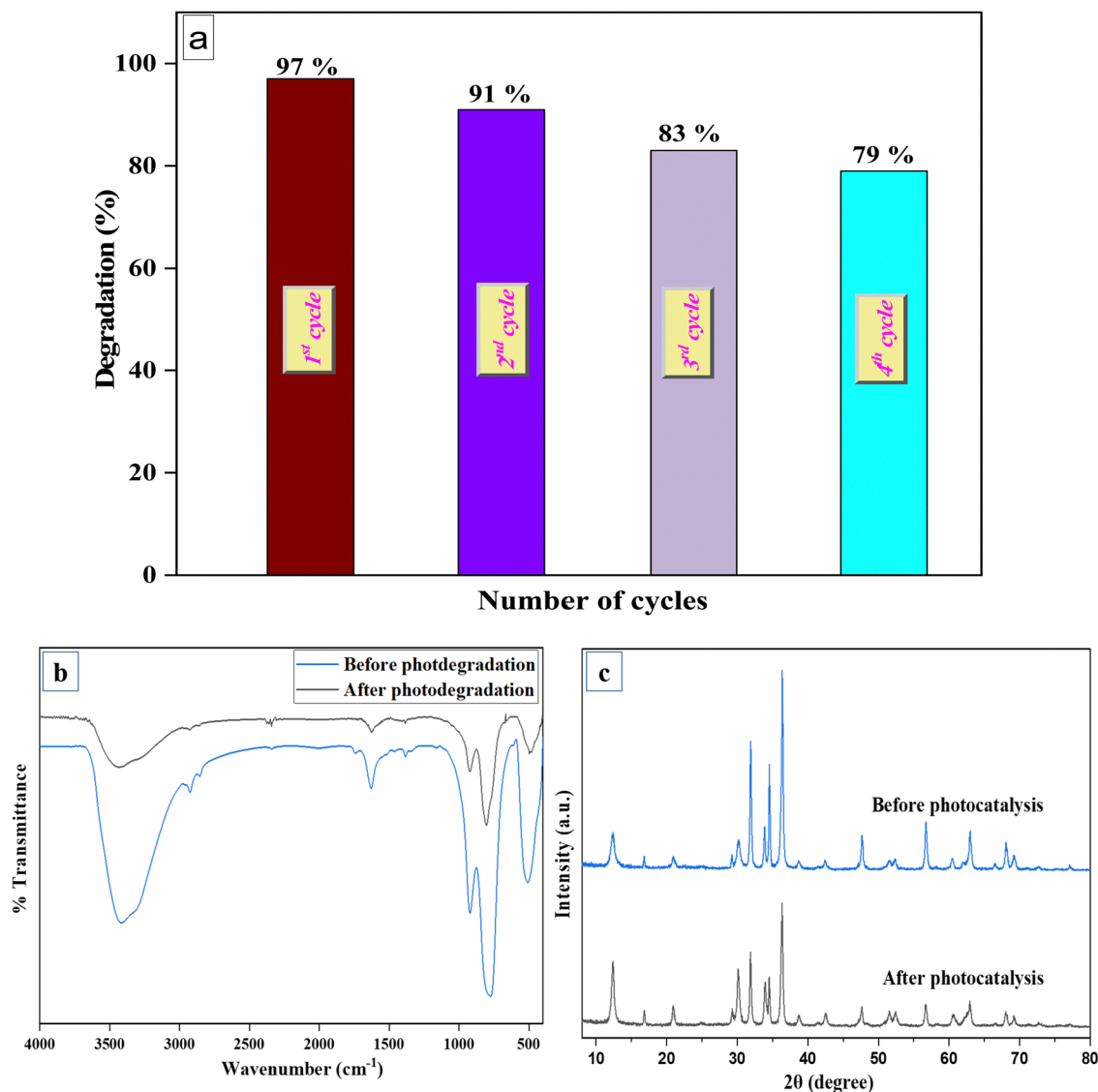


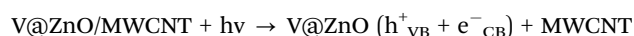
Fig. 15 Recyclability of 6% V@ZnO/MWCNT for the removal of pollutants up to four repeated cycles (a), FTIR spectra (b), and XRD patterns (c) of the binary nanocomposite V@ZnO/MWCNT.

comes under the light source, the electrons get excited from the VB to the CB, leaving the holes in the VB. At that moment, the excited electrons can either be recombined or captured by other species; here, the MWCNTs would play a vital role in rapidly transferring the electrons, and thereby the back electron transfer can be avoided. On the other hand, the excited electrons from the VB of ZnO are accumulated in the CB followed by the V ion impurity level, while leaving the holes in the VB. In this way, the advantage of the introduction of V ions and MWCNTs is that it may involve the reduction of the bandgap energy and separation of photo-generated charge carriers, respectively, therefore extending the lifetime of charge carriers for pollutant degradation. The excited electrons in the CB of ZnO could react directly with oxygen to give $O_2^{\bullet-}$ radicals and the VB holes have strong oxidation potential that can directly react with H_2O molecules to produce $\bullet OH$ radicals.^{63,64} Therefore, to enhance the photodegradation performance of the 6% V@ZnO/MWCNT nanocomposite, the electron transfer

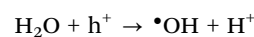
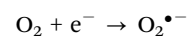
mechanism (Scheme 1) may be accountable for separating charge-carriers and emphasizes the importance of the photocatalytic activity for the degradation of pollutants in wastewater.

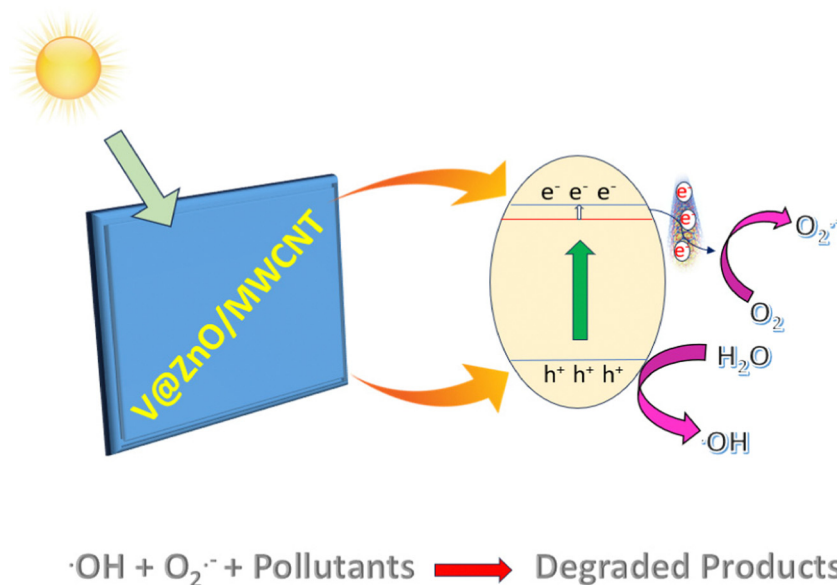
Therefore, based on the above discussion, a plausible photocatalytic degradation mechanism of the 6% V@ZnO/MWCNT nanocomposite (Scheme 1), which may be accountable for separating charge-carriers and emphasizes the importance of the photocatalytic activity for the degradation of pollutants in wastewater.

Step 1: Electron hole-pair generation

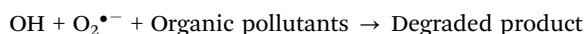


Step 2: Reduction and oxidation process





Scheme 1 A plausible photocatalytic mechanism for pollutant degradation over 6% V@ZnO/MWCNT.



Furthermore, a probable degradation mechanistic pathway for 5-nitroisophthalic acid, allopurinol, and chloramine-T on the irradiated 6% V@ZnO/MWCNT surface in aqueous suspension involving $\bullet\text{OH}$ radicals and $\text{O}_2^{\bullet-}$ radical anions is shown in Scheme S1–S3 (ESI[†]).

5. Conclusion

The findings of this study reveal that amongst all the synthesized materials, the 6% V@ZnO/MWCNT nanocomposite can effectively catalyze the photocatalytic degradation of 5-nitroisophthalic acid, chloramine-T, and allopurinol in aqueous suspension under a UV light source. The results of these studies indicate the significance of selecting the optimal conditions for degradation in order to achieve high efficiency, which is necessary for the functional implementation of oxidative processes. The decomposition of all three model compounds follows pseudo-first-order kinetics and increases in the presence of an electron acceptor like potassium bromate over the most active 6% V@ZnO/MWCNT nanocomposite. From this study, it can also be concluded that the dosage of the photocatalysts, substrate concentration, reaction pH, and additive substances are extremely important parameters for efficiently removing toxic pollutants in water with light under oxygen bubbling. A plausible photocatalytic degradation mechanism pathway over the V@ZnO/MWCNT nanocomposite has been sketched out, which elucidated the intermediate and final products.

Conflicts of interest

The authors declare that they do not have any conflict of interest.

Acknowledgements

The authors acknowledge the Department of Chemistry, AMU, Aligarh for providing all the facilities and DST & UGC for DRS II/PURSE/FIST support to the Department, Aligarh Muslim University.

References

- 1 M. Danish, M. Saud Athar, I. Ahmad, M. Z. A. Warshagha, Z. Rasool and M. Muneer, *Appl. Surf. Sci.*, 2022, **604**, 154604.
- 2 K. M. Lee, C. W. Lai, K. S. Ngai and J. C. Juan, *Water Res.*, 2016, **88**, 428–448.
- 3 S. Wang, Z. Chen, Y. Cai, X.-L. Wu, S. Wang, Z. Tang, B. Hu, Z. Li and X. Wang, *Environ. Funct. Mater.*, 2023, DOI: [10.1016/j.efmat.2023.03.001](https://doi.org/10.1016/j.efmat.2023.03.001).
- 4 X. Liu, Y. Li, Z. Chen, H. Yang, Y. Cai, S. Wang, J. Chen, B. Hu, Q. Huang, C. Shen and X. Wang, *Crit. Rev. Environ. Sci. Technol.*, 2023, **53**, 1289–1309.
- 5 S. R. Mishra and M. Ahmaruzzaman, *Nanoscale*, 2022, **14**, 1566–1605.
- 6 M. S. Athar and M. Muneer, *Photochem. Photobiol. Sci.*, 2022, 1–18.
- 7 S. R. Mishra and M. Ahmaruzzaman, *Sustainable Mater. Technol.*, 2022, **33**, e00463.
- 8 Z. Chen, Y. Li, Y. Cai, S. Wang, B. Hu, B. Li, X. Ding, L. Zhuang and X. Wang, *Carbon Res.*, 2023, **2**, 1–22.
- 9 S. Raha and M. Ahmaruzzaman, *Nanoscale Adv.*, 2022, **4**, 1868.
- 10 J. Li, X. Liu, G. Zhao, Z. Liu, Y. Cai, S. Wang, C. Shen, B. Hu and X. Wang, *Sci. Total Environ.*, 2023, **869**, 161767.
- 11 U. Alam, A. Khan, W. Raza, A. Khan, D. Bahnemann and M. Muneer, *Catal. Today*, 2017, **284**, 169–178.
- 12 A. Sirelkhatim, S. Mahmud, A. Seenii, N. H. M. Kaus, L. C. Ann, S. K. M. Bakhori, H. Hasan and D. Mohamad, *Nano-Micro Lett.*, 2015, **7**, 219–242.



- 13 J.-H. Sun, S.-Y. Dong, J.-L. Feng, X.-J. Yin and X.-C. Zhao, *J. Mol. Catal. A: Chem.*, 2011, **335**, 145–150.
- 14 M. A. Mokammel, M. J. Islam, M. Hasanuzzaman and M. S. J. Hashmi, *Encycl. Smart Mater.*, 2022, 315–324.
- 15 K. Vignesh, M. Rajarajan and A. Suganthi, *J. Ind. Eng. Chem.*, 2014, **20**, 3826–3833.
- 16 K. Umar, A. Aris, T. Parveen, J. Jaafar, Z. Abdul Majid, A. Vijaya Bhaskar Reddy and J. Talib, *Appl. Catal., A*, 2015, **505**, 507–514.
- 17 U. Alam, A. Khan, D. Ali, D. Bahnemann and M. Muneer, *RSC Adv.*, 2018, **8**, 17582–17594.
- 18 U. Alam, T. A. Shah, A. Khan and M. Muneer, *Sep. Purif. Technol.*, 2019, **212**, 427–437.
- 19 S. Kanan, M. A. Moyet, R. B. Arthur and H. H. Patterson, *Catal. Rev.*, 2019, **62**, 1–65.
- 20 V. Vaiano, M. Matarangolo, O. Sacco and D. Sannino, *Appl. Catal., B*, 2017, **209**, 621–630.
- 21 U. Alam, S. Kumar, D. Bahnemann, J. Koch, C. Tegenkamp and M. Muneer, *Phys. Chem. Chem. Phys.*, 2018, **20**, 4538–4545.
- 22 C. Yu, K. Yang, W. Zhou, Q. Fan, L. Wei and J. C. Yu, *J. Phys. Chem. Solids*, 2013, **74**, 1714–1720.
- 23 D. Chen, Y. Cheng, N. Zhou, P. Chen, Y. Wang, K. Li, S. Huo, P. Cheng, P. Peng, R. Zhang, L. Wang, H. Liu, Y. Liu and R. Ruan, *J. Cleaner Prod.*, 2020, **268**, 121725.
- 24 U. Alam, M. Fleisch, I. Kretschmer, D. Bahnemann and M. Muneer, *Appl. Catal., B*, 2017, **218**, 758–769.
- 25 N. Salah, A. Hameed, M. Aslam, S. S. Babkair and F. S. Bahabri, *J. Environ. Manage.*, 2016, **177**, 53–64.
- 26 W. Zhou, Y. Liu, J. Guo and P. Wu, *J. Alloys Compd.*, 2015, **621**, 423–427.
- 27 K. Raja, P. S. Ramesh and D. Geetha, *Spectrochim. Acta, Part A*, 2014, **131**, 183–188.
- 28 S. Rani, P. Suri, P. K. Shishodia and R. M. Mehra, *Sol. Energy Mater. Sol. Cells*, 2008, **92**, 1639–1645.
- 29 Y. Peng, S. Qin, W. S. Wang and A. W. Xu, *CrystEngComm*, 2013, **15**, 6518–6525.
- 30 S. H. Jung, E. Oh, K. H. Lee, Y. Yang, C. G. Park, W. Park and S. H. Jeong, *Cryst. Growth Des.*, 2008, **8**, 265–269.
- 31 R. Mahdavi and S. S. Ashraf Talesh, *Ultrason. Sonochem.*, 2017, **39**, 504–510.
- 32 C. S. Chen, X. D. Xie, T. G. Liu, L. W. Lin, J. C. Kuang, X. L. Xie, L. J. Lu and S. Y. Cao, *J. Nanoparticle Res.*, 2012, **14**, 1–8.
- 33 K. S. Al-Namshah and R. M. Mohamed, *Ceram. Int.*, 2020, **46**, 6914–6919.
- 34 P. Monazzam, A. Ebrahimian Pirbazari and Z. Khodaei, *Mater. Chem. Phys.*, 2019, **228**, 263–271.
- 35 B. Czech and K. Tysczuk-Rotko, *Sep. Purif. Technol.*, 2018, **206**, 343–355.
- 36 M. Danish and M. Muneer, *Ceram. Int.*, 2021, **47**, 13043–13056.
- 37 D. Y. Lee, M. H. Lee, K. J. Kim, S. Heo, B. Y. Kim and S. J. Lee, *Surf. Coat. Technol.*, 2005, **200**, 1920–1925.
- 38 K. Ouyang, S. Xie and X. Ma, *Ceram. Int.*, 2013, **39**, 7531–7536.
- 39 F. X. Xiao, *ACS Appl. Mater. Interfaces*, 2012, **4**, 7055–7063.
- 40 P. Zhang, B. Li, Z. Zhao, C. Yu, C. Hu, S. Wu and J. Qiu, *ACS Appl. Mater. Interfaces*, 2014, **6**, 8560–8566.
- 41 A. J. Reddy, M. K. Kokila, H. Nagabhushana, R. P. S. Chakradhar, C. Shivakumara, J. L. Rao and B. M. Nagabhushana, *J. Alloys Compd.*, 2011, **509**, 5349–5355.
- 42 S. Harish, M. Navaneethan, J. Archana, A. Silambarasan, S. Ponnusamy, C. Muthamizhchelvan and Y. Hayakawa, *Dalton Trans.*, 2015, **44**, 10490–10498.
- 43 X. Q. Wei, Z. G. Zhang, M. Liu, C. S. Chen, G. Sun, C. S. Xue, H. Z. Zhuang and B. Y. Man, *Mater. Chem. Phys.*, 2007, **101**, 285–290.
- 44 P. Bathalavaram, P. Puneetha, S. Ramu, J. Jeon, M. W. Kwon, D. Y. Lee, S. P. R. Mallem, Y. L. Kim and K. Il Park, *Appl. Phys. A: Mater. Sci. Process.*, 2022, **128**, 1–5.
- 45 Q. Deng, X. Duan, D. H. L. Ng, H. Tang, Y. Yang, M. Kong, Z. Wu, W. Cai and G. Wang, *ACS Appl. Mater. Interfaces*, 2012, **4**, 6030–6037.
- 46 M. Caglar and F. Yakuphanoglu, *Appl. Surf. Sci.*, 2012, **258**, 3039–3044.
- 47 Z. L. Wang, X. Y. Kong, Y. Ding, P. Gao, W. L. Hughes, R. Yang and Y. Zhang, *Adv. Funct. Mater.*, 2004, **14**, 943–956.
- 48 J. H. Zheng, J. L. Song, Z. Zhao, Q. Jiang and J. S. Lian, *Cryst. Res. Technol.*, 2012, **47**, 713–718.
- 49 W. Raza, S. M. Faisal, M. Owais, D. Bahnemann and M. Muneer, *RSC Adv.*, 2016, **6**, 78335–78350.
- 50 C. Liu, Y. Qiu, F. Wang, K. Wang, Q. Liang and Z. Chen, *Adv. Mater. Interfaces*, 2017, **4**, 1700681.
- 51 C. Ren, B. Yang, M. Wu, J. Xu, Z. Fu, Y. Lv, T. Guo, Y. Zhao and C. Zhu, *J. Hazard. Mater.*, 2010, **182**, 123–129.
- 52 Y. Suchorski, L. Rihko-Struckmann, F. Klose, Y. Ye, M. Alandjiyska, K. Sundmacher and H. Weiss, *Appl. Surf. Sci.*, 2005, **249**, 231–237.
- 53 M. E. Harlin, V. M. Niemi and A. O. I. Krause, *J. Catal.*, 2000, **195**, 67–78.
- 54 W. Xiong, G. Zeng, Z. Yang, Y. Zhou, C. Zhang, M. Cheng, Y. Liu, L. Hu, J. Wan, C. Zhou, R. Xu and X. Li, *Sci. Total Environ.*, 2018, **627**, 235–244.
- 55 A. Eatemadi, H. Daraee, H. Karimkhanloo, M. Kouhi, N. Zarghami, A. Akbarzadeh, M. Abasi, Y. Hanifehpour and S. W. Joo, *Nanoscale Res. Lett.*, 2014, **9**, 1–13.
- 56 R. Konnola and K. Joseph, *RSC Adv.*, 2016, **6**, 23887–23899.
- 57 X. Shi, X. Zhang, F. Bi, Z. Zheng, L. Sheng, J. Xu, Z. Wang and Y. Yang, *J. Mol. Liq.*, 2020, **316**, 113812.
- 58 S. B. Somvanshi, S. A. Jadhav, M. V. Khedkar, P. B. Kharat, S. D. More and K. M. Jadhav, *Ceram. Int.*, 2020, **46**, 13170–13179.
- 59 J. Chen, X. Zhang, X. Shi, F. Bi, Y. Yang and Y. Wang, *J. Colloid Interface Sci.*, 2020, **579**, 37–49.
- 60 J. Chen, X. Zhang, F. Bi, X. Zhang, Y. Yang and Y. Wang, *J. Colloid Interface Sci.*, 2020, **571**, 275–284.
- 61 M. S. Athar and M. Muneer, *Photochem. Photobiol. Sci.*, 2022, **1**, 1–18.
- 62 M. Lindner, D. W. Bahnemann, B. Hirthe and W. D. Griebler, *J. Sol. Energy Eng.*, 1997, **119**, 120–125.
- 63 U. Alam, S. Kumar, D. Bahnemann, J. Koch, C. Tegenkamp and M. Muneer, *Phys. Chem. Chem. Phys.*, 2018, **20**, 4538–4545.



- 64 N. O. Balayeva, M. Fleisch and D. W. Bahnemann, *Catal. Today*, 2018, **313**, 63–71.
- 65 M. S. Athar, M. Danish and M. Muneer, *J. Environ. Chem. Eng.*, 2021, **9**, 105754.
- 66 V. Gadore, S. R. Mishra and M. Ahmaruzzaman, *J. Hazard. Mater.*, 2023, **444**, 130301.
- 67 S. Begum, S. R. Mishra and M. Ahmaruzzaman, *Environ. Sci. Pollut. Res.*, 2022, **29**, 87347–87360.

